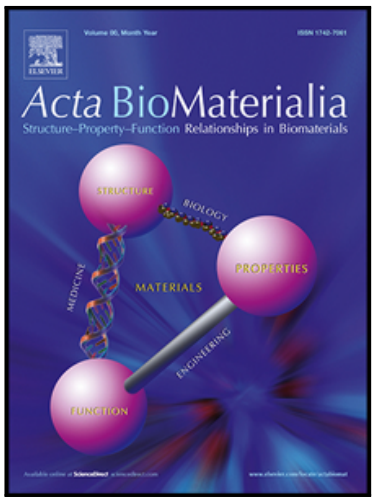

Construction of a Core-shell Microneedle System to Achieve Targeted Co-delivery of Checkpoint Inhibitors for Melanoma Immunotherapy

Peipei Yang , Chao Lu , Wanbing Qin , Minglong Chen , Guilan Quan , Hu Liu , Lili Wang , Xuequn Bai , Xin Pan , Chuanbin Wu

PII: S1742-7061(19)30880-3
DOI: https://doi.org/10.1016/j.actbio.2019.12.037
Reference: ACTBIO 6520

To appear in: *Acta Biomaterialia*

Received date: 8 September 2019
Revised date: 23 December 2019
Accepted date: 29 December 2019

Please cite this article as: Peipei Yang , Chao Lu , Wanbing Qin , Minglong Chen , Guilan Quan , Hu Liu , Lili Wang , Xuequn Bai , Xin Pan , Chuanbin Wu , Construction of a Core-shell Microneedle System to Achieve Targeted Co-delivery of Checkpoint Inhibitors for Melanoma Immunotherapy, *Acta Biomaterialia* (2020), doi: https://doi.org/10.1016/j.actbio.2019.12.037

Full length article

Construction of a Core-shell Microneedle System to Achieve Targeted Co-delivery of Checkpoint Inhibitors for Melanoma Immunotherapy

Peipei Yang[a,c,#], Chao Lu[a,b,#], Wanbing Qin[a], Minglong Chen[a], Guilan Quan[a,b], Hu Liu[d], Lili Wang[d], Xuequn Bai[a], Xin Pan[a,], Chuanbin Wu[a,b,*]*

[a] School of Pharmaceutical Sciences, Sun Yat-sen University, Guangzhou 510006, China

[b] College of Pharmacy, Jinan University, Guangzhou 510632, China

[c] Guangzhou Women and Children's Medical Center, Guangzhou 510623, China

[d] School of Pharmacy, Memorial University of Newfoundland, St. John's, Newfoundland and Labrador A1B3V6, Canada

***Corresponding author**

Chuanbin Wu, Ph.D.

School of Pharmaceutical Sciences, Sun Yat-sen University, Guangzhou 510006, China

College of Pharmacy, Jinan University, Guangzhou 510632, China

Phone: (86)-20-39943120

E-mail: wuchuanb@mail.sysu.edu.cn

Xin Pan, Ph.D.

School of Pharmaceutical Sciences, Sun Yat-sen University, Guangzhou 510006, China

Phone: (86)-20-39943427

E-mail: panxin2@mail.sysu.edu.cn

 # These authors contributed equally to this work.

Abstract: Synergistic anti-tumor effect of anti-PD-1/L1 antibody (aPD-1/aPD-L1) and 1-methyl-D,L-tryptophan (1-MT) in melanoma has been well demonstrated, while efficient topical delivery systems are still largely unexplored. Here, a highly drug-concentrated hybrid core-shell microneedle (CSMN) system for co-delivery of checkpoint inhibitors was developed. Based on the specific drug-matrix interaction, the system concentrated aPD-L1 in the tips of microneedles through electrostatic interactions, and increased the amount of 1-MT loaded in CSMN by preventing its premature crystallization using PVA, the material used to prepare CSMN core. The prepared CSMN exhibited high transdermal delivery efficiency and long topical retention time of aPD-L1 for 2 days. Drug-loaded CSMN achieved better anti-tumor efficacy than the intra-tumor injection group at the same dose, which was likely because the former recruited more T lymphocytes to the tumor site. These findings suggested that this CSMN system was a promising local delivery system of both aPD-L1 and 1-MT for melanoma immunotherapy, and its unique core-shell structure could be readily adapted as a modular platform for various diseases, where combination therapy of both biomacromolecular drugs and other small-molecular agents were required.

Statement of significance

In the present study, a core-shell microneedle (CSMN) system was constructed to achieve targeted co-delivery of checkpoint inhibitors to melanoma, while preventing significant systemic exposure. To overcome the drawback of insufficient drug loading of microneedles and effectively encapsulate two drugs simultaneously, microneedles were divided into two independent functional areas, a charged shell and a hydrophilic core and encapsulated drugs based on respective drug-matrix interaction. The charged shell prepared by chitosan could

concentrate aPD-L1 in the tips of microneedles through electrostatic interactions. The core prepared by PVA successfully increased the amount of 1-MT loaded in microneedles by preventing its premature crystallization. The prepared CSMN exhibited high transdermal delivery efficiency and better anti-tumor efficacy than intra-tumor injection at the same dose.

Keywords: Core-shell microneedle; Immunotherapy; Melanoma; Anti-PD-L1 antibody; IDO inhibitor

1. Introduction

Melanoma is one of the most aggressive cancers occurred at the superficial skin with increasing incidence and mortality over the past decades [1-2]. It readily metastasizes, limiting the efficacy of traditional treatments including surgery and radiotherapy. Chemotherapy is, therefore, the most common treatment, but it usually causes toxic effects and lacks long-term responses in patient [3]. It was reported that spontaneous regression accompanied by T lymphocytes infiltration occurred in melanoma, which indicated the potential of immunotherapy of melanoma [4]. However, cytotoxic immune attack is often found to be inhibited by the presence of immune checkpoints in the tumor microenvironment, which is known as tumor immune escape [5-7]. One of the known immune check points is the interaction between programmed cell death receptor-1 (PD-1) found on the surface of activated anti-tumor cytotoxic T-cells and its ligand, PD ligand 1 (PD-L1) found to be over-expressed on the surface of many tumor cells [8-9]. Once PD-1 is bound to PD-L1, T-cells would undergo apoptosis and its immune cytotoxic effects would be dissipated [10]. Besides, immunoregulatory enzyme indoleamine 2,3-dioxygenase and tryptophan-2,3-dioxygenase (IDO/TDO) are also highly

expressed in tumor microenvironment. They can rapidly convert tryptophan (Try) to kynurenine (Kyn), resulting in suppression of T-cells activation and insufficient ability to kill tumor cells [11]. To restore the cytotoxic effect of activated cytotoxic T-cells against tumor cells, antibodies against PD-1/L1 (aPD-1/L1) can be used to block the interaction between PD-1 and PD-L1, while IDO/TDO pathway inhibitors can be applied to inhibit the IDO/TDO activity [6, 12]. Since multiple immune inhibitory mechanisms present concurrently in the tumor microenvironment, the clinical benefit of single checkpoint inhibitor is limited. It has been reasoned that combination therapies may be required for optimal therapeutic effect [13-14]. In contrast to selective IDO1 enzyme inhibitors, indoximod targets a downstream effector molecule mTORC1 of all IDO/TDO enzymes, possibly lowering risks of drug resistance caused by IDO1 bypass [15]. A recent phase Ⅱ clinical trial has demonstrated the synergistic anti-tumor effect of aPD-1/ aPD-L1 and indoximod in advanced melanoma [16].

Systemic exposure of checkpoint inhibitors may give rise to a series of adverse events due to off-target effects [17]. Local administration to melanoma can achieve targeted delivery with reduced systemic exposure and improved bioavailability [18]. However, stratum corneum is the major barrier for efficient transdermal drug delivery to local lesions, especially for biomacromolecules. Dissolving microneedle system is an ideal transdermal delivery system, which can create an array of microchannels in the epidermis and dermis in a minimally invasive manner to facilitate the transdermal delivery of small molecules, biomacromolecules and even nanoparticles [19-21]. The materials used to prepare microneedles are highly biocompatible, which could dissolve or degrade in the skin. In addition, microneedles encapsulate biomacromolecules in a dried solid form, which provides enhanced drug stability and reduces the use of cold chain [22]. Recent studies have demonstrated the potential of microneedles as a

delivery system for chemotherapy, photothermal therapy and immunotherapy of tumors [23-27]. For example, Gu *et al* developed microneedle systems to deliver aPD-L1 alone or with an IDO inhibitor 1-MT simultaneously for melanoma treatment with an enhanced efficacy compared to intratumoral and intravenous injection [26-27].

Although microneedles exhibit great potential in local delivery for tumor immunotherapy, with its microstructure of small volume, the amount of drug loaded in traditional microneedle is limited. The diffusion of aPD-L1 during microneedle preparation process and the poor water solubility of 1-MT in the needle matrix solution make it more challenging for sufficient encapsulation [28-29]. Notably, traditional microneedles are failed to concentrate drug in the microneedle tips, so they are difficult to achieve completely transdermal delivery because of the elastic deformation of skin. Moreover, since the needle part of traditional microneedle is usually prepared by homogeneous material, synchronous encapsulation of multi-agents based on specific drug-matrix interaction is restricted. By contrast, with two-layer hybrid structure, core-shell microneedle (CSMN) provides a more functional platform for customized drug encapsulation. According to the physicochemical characteristics of different drugs, such as charge, hydrophilicity and contents of hydrogen bond donors/acceptors, the matrix material of each layer can be customized to optimize the drug loading efficiency, stability and release behavior.

In the present study, a CSMN system consisting of a charged shell and a hydrophilic core capable of forming hydrogen bonds was developed to achieve co-delivery of aPD-L1 and 1-MT with improved drug loading (Fig. 1). The charged shell could adsorb aPD-L1 through a strong electrostatic interaction to reduce its diffusion during preparation and concentrate it in microneedle tip. Polymers rich in hydrogen bond donors and acceptors such as polyvinyl alcohol (PVA) were used as the materials for the core of microneedles. They were found to inhibit the

premature crystallization of 1-MT and maintain its concentration at the supersaturated state through forming hydrogen bonds with 1-MT. The homogeneous and supersaturated drug-polymer solution should be beneficial for making uniform microneedles with increased drug amounts. The ability of different polymers to form supersaturated 1-MT solutions was compared. The formation of the shell and the loading efficiency of aPD-L1 in the shell were examined using a series of techniques. The skin insertion ability and transdermal delivery efficiency of CSMN were investigated. Finally, the anti-tumor efficacy of the CSMN system in a subcutaneous melanoma C57BL/6 mice model was evaluated. The type and proportion of infiltrating lymphocytes at the tumor microenvironment were also examined in order to understand the mechanisms of immunotherapy.

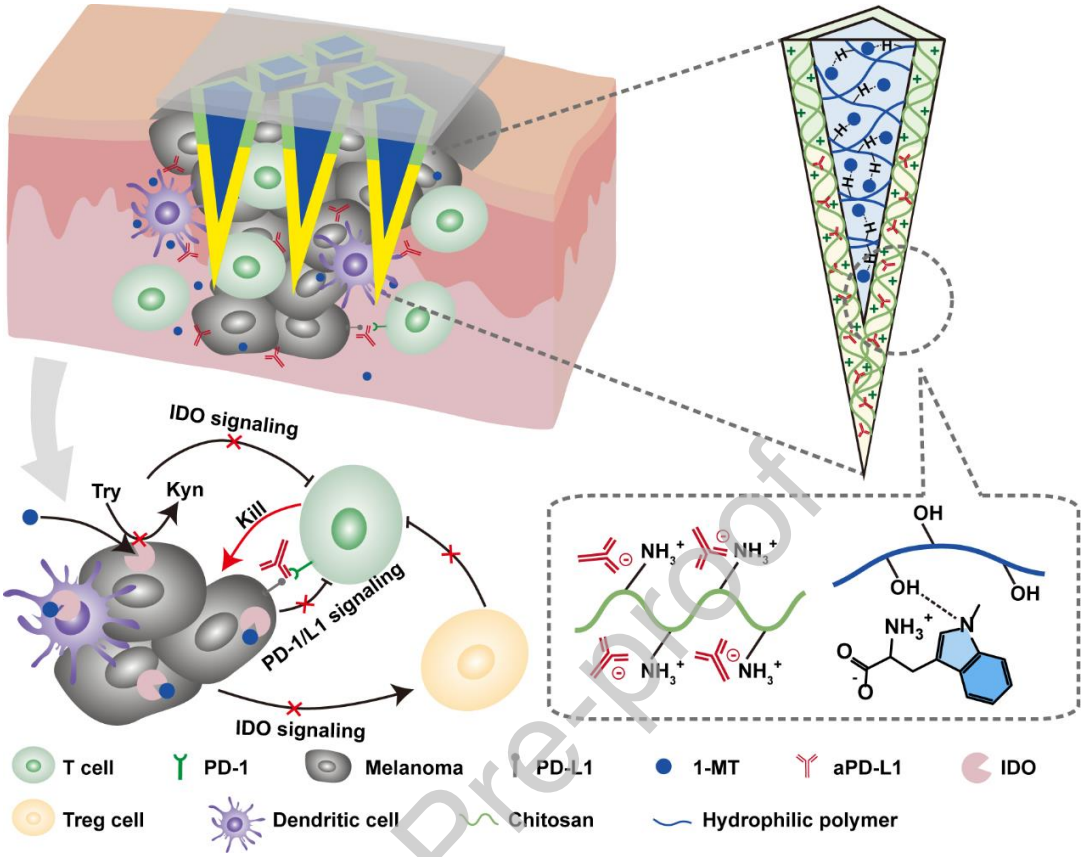

Fig. 1.

2. Materials and methods

2.1. Materials

PVA 103, dextran (DEX, M_w = 40,000) and polyethylene glycol (PEG, M_w = 8,000) were purchased from Aladdin. Poly (N-vinylpyrrolidone) (PVP) K30 and K90 were kindly provided by BASF. Oligomeric sodium hyaluronate (HA) was purchased from Bloomage Freda Biopharm Co., Ltd. Chitosan (CS, M_w = 50,000) was purchased from Zhejiang Golden-shell Pharmaceutical Co., Ltd. Sodium alginate (ALG, low viscosity) was purchased from J&K Scientific. Anti-PD-L1 antibody was purchased from Biolegend Inc. (cat. no. 124329, clone: 10F.9G2), while 1-MT was purchased from Shanghai Superlan Chemical Co., Ltd. Staining

antibodies used for flow cytometry including anti-CD3-FITC (Clone: 17A2, Catalog: 11-0032-82), anti-CD8a-PE (Clone: 53-6.7, Catalog: 12-0081-81) and anti-CD4-APC (Clone: RM4-5, Catalog: 17-0042-81) antibodies were purchased from eBioscience Inc.

2.2. Effect of polymers on the crystallization of 1-MT

Supersaturated 1-MT solutions containing PVA, DEX, PVP K30, HA or PEG were prepared, respectively. The obtained solutions were placed in a gas bath thermostatic oscillator maintained at 37°C and 100 rpm. The concentration of 1-MT in the supersaturated solutions in 24 h after their preparation was quantified by high performance liquid chromatography (HPLC). To confirm the inhibition effect of polymers on the crystallization of 1-MT, solution samples were also observed under a polarized light microscope (LV100POL, Nikon).

2.3. Fabrication of CSMNs

CSMNs were prepared by centrifugation molding technology using polydimethylsiloxane (PDMS) female molds containing microcavities inversely replicated from the brass master structures (Fig. 2). Microneedles were in pyramid shape with a square base of 300 μm by 300 μm and a height of 800 μm and were arranged in a 12 by 12 array with a 750 μm center-to-center spacing on a 9×9 mm^2 patch. In all experiments except for the *in vivo* immune therapy experiments in mice, bovine serum albumin (BSA) was used as a model protein drug due to the cost of aPD-L1.

The shell of CSMN was first prepared by pipetting chitosan solution or sodium alginate solution onto the surface of each PDMS mold followed by centrifugation at 4,000 rpm for 5 min at 0-10°C. Residual solution outside of the microcavities was removed. Then the molds were

centrifuged twice at 4,000 rpm for 30 min at 20-30°C with the molds being rotated 180° at the second time. After that, the molds were dried in a sealed container containing allochroic silica gel for 12 h for the CSMN shells to harden. CSMN with shell prepared by chitosan or alginate was defined as CS-CSMN or ALG-CSMN.

The molds were covered with aPD-L1 or BSA solution followed by centrifugation twice at 4,000 rpm for 2 min at 0-10°C. During the first spin, only half of each mold was covered. Then the molds were rotated 180° to cover the other halves during the second spin. The two centrifugation steps were necessary to ensure that the aPD-L1 or BSA solution completely filled all microcavities. After removing the excess aPD-L1 or BSA solution on the surface, the molds were centrifuged again at 4,000 rpm for 30 min at 20-30°C and then dried in a desiccator for 12 h.

To fabricate the core of CSMN, aqueous solution consisting of 15% (w/v) PVA and 25% (w/v) PVP K30 with 15 mg/mL 1-MT was poured on the surface of the molds and centrifuged at 4,000 rpm for 5 min at 0-10°C. Overflowing solution was scraped away. The base solution (PVP K90 dissolved in ethanol, 31.25%, w/v) was added and centrifuged under the same conditions to form the CSMN base. After being dried in a desiccator for 72 h at room temperature, CSMN was gently separated from the molds and stored in an airtight container. To measure the amount of aPD-L1 or BSA loaded in the CSMN, all needles were separated from the patch with a razor blade and dissolved in 1% (w/v) acetic acid. The amount of aPD-L1 or BSA was measured by Coomassie brilliant blue method and calculated in accordance with the standard curve. To measure the loading amount of 1-MT, needles were dissolved in deionized water and HPLC analysis was conducted.

Microneedles without shell (nMN) were prepared following the same preparation process without the shell preparation step. The fluorescent microneedles were also prepared with FITC-labeled chitosan, FITC-labeled or TRITC-labeled BSA and a Cyanine fluorescent dye (Cy5) to replace 1-MT and visualize the core of CSMN. The core-shell structure and drug distribution in CSMN were observed by laser scanning confocal microscope (FV3000, Olympus) and stereoscopic fluorescence microscope (Lumar.V12, Zeiss).

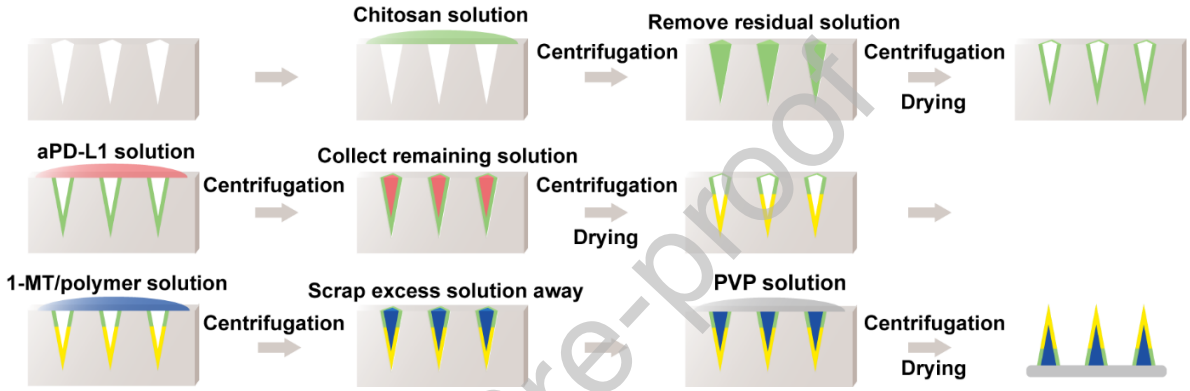

Fig. 2.

2.4. *In vitro* skin insertion test

CS-CSMN and fluorescent CS-CSMN were inserted into the excised abdominal skin of Sprague−Dawley rats by thumb pressure for 2 min. Before CS-CSMN was applied, the hair on the skin was carefully shaved by a razor followed by application of depilatory cream. Trypan blue staining was performed to reveal the holes remaining in the skin after CS-CSMN removal. The skin site inserted by CS-CSMN was fixed in 4% paraformaldehyde, embedded in paraffin and sliced into 5 μm sections and then stained by hematoxylin and eosin (H&E). For the site inserted by fluorescent CS-CSMN, cross-section of the skin was prepared by cryotomy. To visualize the depth of CS-CSMN insertion into the skin, skin samples were observed under an optical coherence tomography scanner (OCT) 1 min after CS-CSMN administration. The

insertion depth was further confirmed by conducting confocal laser scanning along z axis on the skin after removal of fluorescent CS-CSMN.

2.5. *In vitro* skin permeation study

In vitro transdermal delivery of 1-MT by three different microneedles was evaluated using a Franz diffusion cell apparatus. Abdominal skin of Sprague−Dawley rat was excised and the subcutaneous fat was carefully removed. After the insertion of microneedles, skin was fixed in the cell with dermis in contact with phosphate buffered saline (PBS, pH 5.8) in the receptor chamber. The receptor solution was magnetically stirred at 250 rpm and maintained at 37°C. At the predetermined time intervals, aliquots of receptor solution samples were withdrawn and the 1-MT concentration was measured.

2.6. Protein retention time and chitosan shell degradation in skin

To determine the transdermal delivery efficiency and skin retention time of proteins, and degradation time of chitosan shell in the skin, TRITC-labeled BSA loaded nMN and CS-CSMN or CSMN prepared by FITC-labeled chitosan were applied to the back skin of C57BL/6 mice after hair removal. After treatment for 30 minutes, microneedles were removed and skin treated with microneedles was wiped gently using a cotton swab to remove BSA-TRITC or CS-FITC remaining on the surface. Fluorescence intensity of the treated regions was monitored by an *in vivo* imaging system (NightOWL Ⅱ LB983, Berthold) for 2 days.

2.7. *In vivo* anti-tumor efficacy and safety

All animal experiments were conducted according to the protocol approved by the Institutional Animal Care and Use Committee of Sun Yat-sen University. Female C57BL/6 mice (6-7 weeks old) were kept in pathogen-free conditions with a 12 h/12 h light/dark cycle and free access to food and water. The subcutaneous melanoma mice model was established by subcutaneous injection of 1×10^6 of B16 cells at the dorsal flank of C57BL/6 mice after hair removal. When the volume of subcutaneous tumors reached 50−60 mm^3, the mice were randomly divided into 3 groups (9 mice/ group), receiving a piece of blank CS-CSMN, aPD-L1/1-MT CS-CSMN or intra tumor injection of aPD-L1/1-MT solution (4.4 μg of aPD-L1 and 36 μg of 1-MT per mice), respectively. Microneedle patches were applied to the tumor site for 2 min and further fixed using medical adhesive tape for 30 min. The tumor size of 6 mice was evaluated by measuring the long diameter and short diameter of tumor using a digital caliper every two days and calculated as long diameter × short diameter × short diameter/2. To reveal the mechanisms of tumor regression, tumors of 3 mice in different groups were harvested 12 days after treatment and prepared into single-cell suspensions followed by removing red blood cells (RBC) using the RBC lysis buffer. The type and proportion of tumor infiltrating lymphocytes were analyzed by flow cytometry (CytoFLEX, Beckman Coulter) after being stained with anti-CD3-FITC, anti-CD8a-PE and anti-CD4-APC antibodies. To assess the potential toxicity of CSMN, the weight loss of mice after treatment was monitored every two days, and histopathology analysis was conducted on the major organs.

2.8.Statistical analysis

Data are presented as mean ± standard deviation (SD). Statistical significance of tumor size and tumor infiltrating lymphocytes of mice receiving different treatments were calculated by one-way ANOVA using the LSD post-test following normality and equal variance tests (SPSS

22.0). Comparisons of survival curves were made using the log-rank test. *P*-values <0.05 was considered to indicate statistically significant differences. **P* < 0.05; ***P* < 0.01; ****P* < 0.001.

3. Results and discussion

3.1. Inhibition effect of polymers on the crystallization of 1-MT

The drug loading amount in the microneedle core is usually limited by the poor drug solubility in the microneedle preparation solutions [29]. 1-MT, an IDO inhibitor, has a similar structure to tryptophan, an aromatic amino acid. It is slightly soluble in water while soluble in alkaline and acidic conditions. Using of supersaturated formulations results in drug concentrations exceeding the equilibrium solubility. However, supersaturated solutions are thermodynamically unstable which leads to the formation of crystal nuclei followed by crystal growth. It has been demonstrated that polymer based crystallization inhibitors could effectively retard the crystallization process, maintaining drug concentrations at the supersaturated state for an extended period of time by hydrogen bonding, hydrophobic interactions or increased viscosity [30]. However, the most effective inhibitor and concentration vary depending on the drug [31].

Since both of its amino and carboxyl groups are ionized, 1-MT molecule has only one hydrogen bond acceptor (indolyl nitrogen) with no hydrogen bond donor available. In this study, various polymers rich in hydrogen bond donors (hydroxyl), such as PVA, DEX and HA, were used to prepare supersaturated 1-MT solutions and their ability in inhibiting the crystallization of 1-MT was compared by determining the apparent 1-MT concentration-time profiles. As shown in Fig. 3a, PVA demonstrated a superior ability compared to other polymers in maintaining the supersaturated state of 1-MT. The initial concentration of 1-MT in its supersaturated solution was maintained for 4 h with more than 95% of its initial concentration left at 8 h in the presence

of PVA, while it began to decline 2 h after its preparation in the presence of DEX, indicating a weaker ability of DEX than PVA in inhibiting 1-MT crystallization. HA exhibited little ability in maintaining the supersaturated state of 1-MT solution showing a gradual decrease of 1-MT concentration over time. The results are believed to be related to the hydroxyl contents of the polymers used, which are 2.27 mol/100 g, 1.85 mol/100 g and 1.06 mol/100 g for PVA, DEX and HA, respectively. It appears that higher hydroxyl contents likely result in more hydrogen bonds between 1-MT and the polymer, which increase the nucleation activation energy and delay the nucleation. In addition, polymers may form a protective layer around the newly-formed crystals through hydrogen bonds formed between polymers and crystal surface to inhibit crystal growth [30]. The ability of PVP and PEG to maintain the supersaturated state of 1-MT was also investigated. Like 1-MT, both materials are rich in hydrogen bond acceptors with no hydrogen bond donor sites available. Therefore, hydrogen bonding can't be established. The results showed that PEG failed to inhibit or retard crystallization. However, PVP showed some ability in maintaining the supersaturated state of 1-MT for the first 4 hours, which may be attributed to its high molecular weight and viscosity.

The inhibition effect of PVA on the crystallization of 1-MT was found to be influenced by the concentrations of PVA and 1-MT (Fig. 3b). The duration of the supersaturated state was proportional to the concentration of the polymer. 1-MT was found to be at the concentration of 12 mg/mL for 24 h by 15% PVA, while only for 2 h by 5% PVA. As the original concentration of 1-MT increased, the duration of supersaturated state maintained by PVA decreased. When the initial concentration of 1-MT was increased from 12 mg/mL to 15 mg/mL, the duration of the supersaturated state maintained by 15% PVA was shortened from 24 h to 8 h. It should be noted that 8 h is practically long enough for the microneedle preparation. PVA showed a very poor

supersaturation inhibition effect as 1-MT concentration increased to 18 mg/mL. Thus, the concentration of 15 mg/mL was selected as the optimum 1-MT concentration in this study. The polarized light microscopy images also confirmed the effect of polymers on the 1-MT crystallization from its supersaturated solutions. As shown in Fig. 3c, 1-MT crystallized rapidly and formed many large crystals at the concentration of 12 mg/mL in the first 15 min in the absence of polymers, while no crystal was observed until 36 h in the presence of 15% PVA.

PVA is a kind of material with high toughness and low hardness. Microneedles prepared only with PVA performed poorly on skin insertion [32]. Many studies demonstrated that PVP K30 was a suitable material to mix with PVA to enhance mechanical strength of microneedles [33-34]. The effect on 1-MT crystallization in the presence of both PVA and PVP K30 was investigated. Results showed that their co-presence extended the duration time of 1-MT supersaturated state at the concentration of 12 mg/mL and 15 mg/mL to 60 h and 36 h, respectively (Fig. 3c).

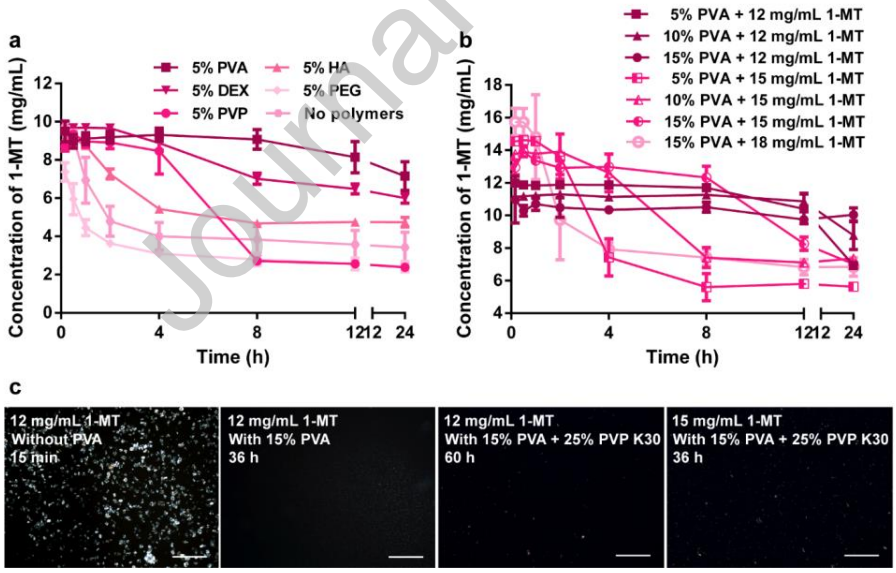

Fig. 3.

3.2. Fabrication of CSMNs

The CSMN were prepared through the layer-by-layer technology, consisting of a shell containing aPD-L1 and a hydrophilic core loaded with 1-MT. The shell of CSMNs was firstly prepared following a centrifugation-drying procedure. Then aPD-L1 was adsorbed into the pre-formed shell. Fifteen percent PVA was selected as core material and mixed with 25% PVP K30 to help with the formation of supersaturated 1-MT solution and the mechanical strength of CSMN core.

To validate the successful formation of the external shell of CSMN, FITC-labeled chitosan was used to prepare the shell of CSMN. A complete shell structure covering the whole microneedles was formed when the concentration of chitosan solution was more than 6 mg/mL (Fig. 4a and 4b), while 2 mg/mL chitosan solution failed to produce an intact CSMN shell with chitosan found only in the tips of microneedles. As expected, the amount of BSA loaded in the CSMNs with shells prepared by 6-10 mg/mL chitosan solution was doubled, compared to that of nMN (Fig. 4c). However, 2 mg/mL chitosan solution only slightly increased the BSA loading efficiency in microneedles since it only covered the tips of microneedles. The mechanism for the increased protein loading was likely attributed to the strong electrostatic forces between the positively charged chitosan and the negatively charged protein. As a result, protein could likely be adsorbed and condensed in the shell instead of being re-dissolved in the core preparation solution, subsequently overflowing from the microcavities of molds and even being scraped away. Because 10 mg/mL chitosan solution was able to form a denser shell than 6 mg/mL chitosan solution, it was used for further studies (Fig. 4b). The loading efficiency in the shell reached as high as more than 80% when the BSA concentration was 1-3 mg/mL (Fig. S1).

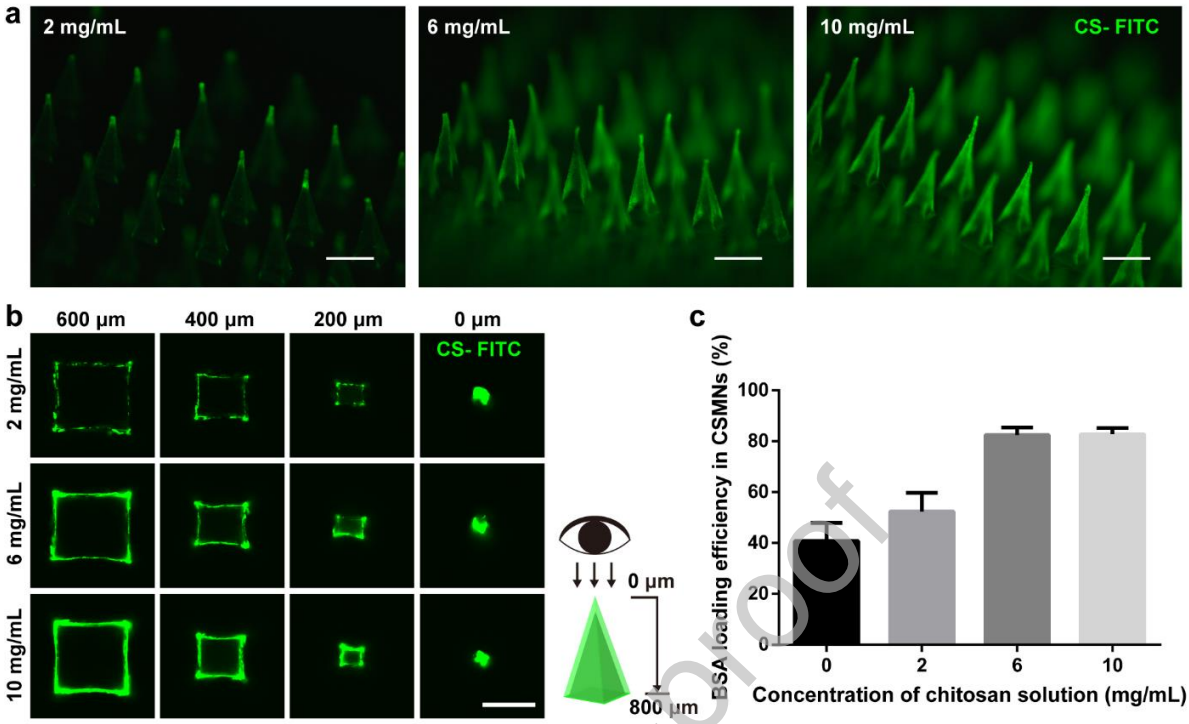

Fig. 4.

Although negatively charged, sodium alginate was also found to improve the aPD-L1 loading in the microneedles with a loading efficiency of nearly 70%, similar to that of CS-CSMN (Fig. 5c). The results are likely due to the electrostatic interactions of sodium alginate and the positively charged amino acid residues or domains of the aPD-L1. As shown by fluorescent microscopy images (Fig. 5a and 5b), FITC-labeled BSA was concentrated in the tips of CS-CSMN or ALG-CSMN, while distributed near the bottom of nMN. This was because that chitosan or alginate would be deposited in the tip part of microneedle mold under centrifugation force, forming a thicker shell at the tip part (Fig. 5d and S2), ultimately leading to the main distribution of BSA in the CSMN tips. For nMN, the pre-loaded BSA would re-dissolve into the needle solution and migrate to the bottom of needle part due to concentration gradient during nMN preparation process (Fig. S3). The differences in BSA distribution confirmed that charged

shell could retard protein diffusion. Because sodium alginate was soluble in water, it might be re-dissolved into aPD-L1 or BSA solution during microneedle preparation, which resulted in less loading of protein than CS-CSMN. It was also found that FITC-labeled BSA distributed near the surface of microneedles forming a shell-like layer in nMN, which was probably attributed to the centrifugation-drying procedure (Fig. 5a). CS-CSMN was used for further study due to its better encapsulation efficiency.

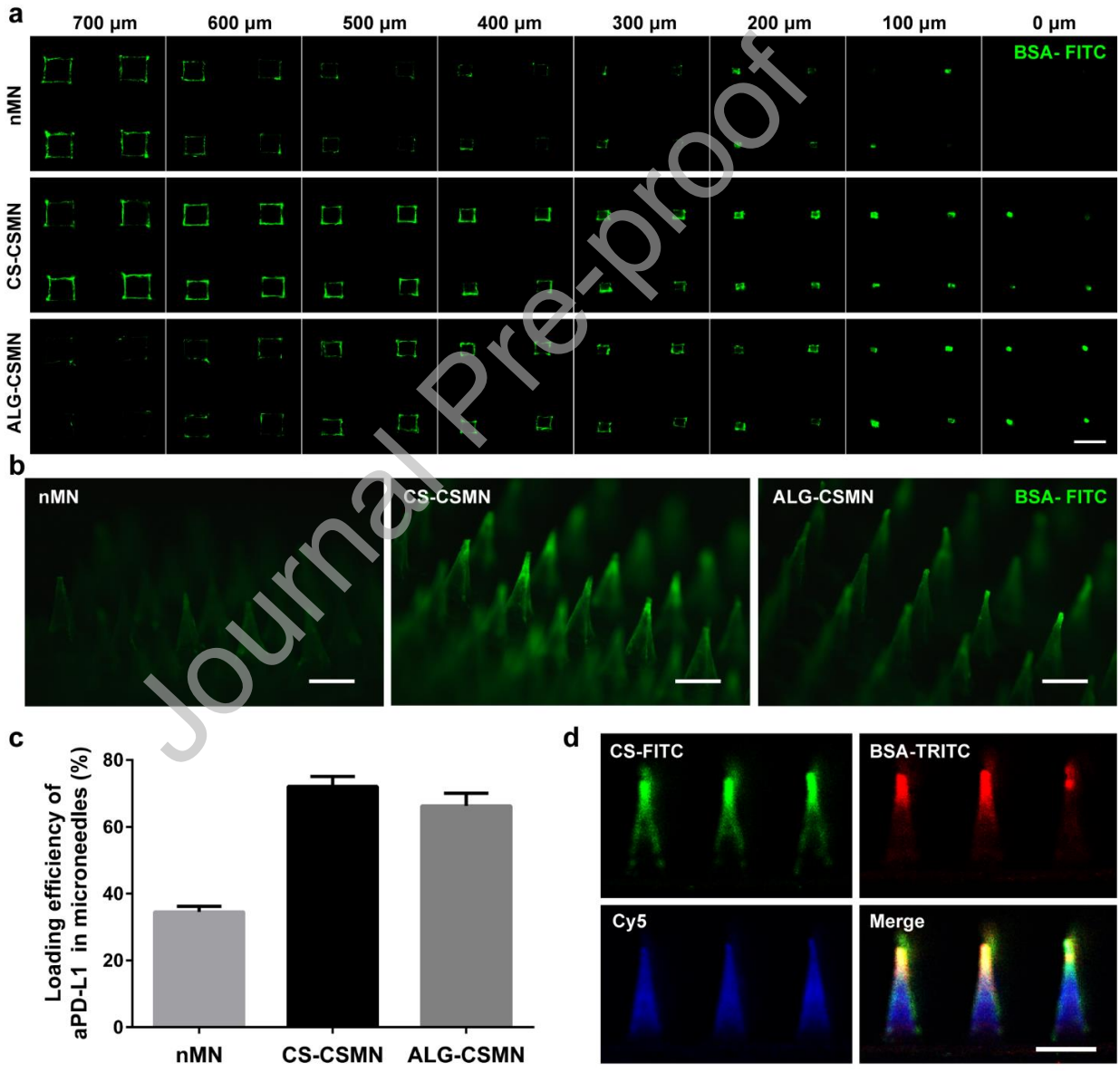

Fig. 5.

3.3. *In vitro* skin insertion test

Fig. 6a was a photograph of a representative CS-CSMN patch. Because chitosan used in this study was golden, the surface of CS-CSMN, especially in the tip, displayed a yellow color (Fig. 6b). As shown in Fig. 6c, 6e and S4, CS-CSMN had enough mechanical strength to penetrate into the rat skin and an array of spots on the skin surface corresponding to CS-CSMN puncture sites were observed. As shown in Fig. 6d, the prepared CS-CSMN was able to penetrate in the corium layer, and the chitosan shell was stained pink by H&E because of its positive charge. The OCT image demonstrated that the CS-CSMN system was completely inserted into the skin, at approximately 770 μm in depth and holes about 300 μm in diameter in the stratum corneum were visible (Fig. 6g). A space of around 100 μm between the bottom of the CS-CSMN base and the upper surface of the stratum corneum was formed along with the dissolution and separation of joint part between needles and base. To further determine the insertion depth of CS-CSMN, the puncture sites on the skin were examined vertically using confocal laser scanning microscopy along z axis from surface to depth of skin. The results showed that the fluorescence signal of CS-FITC decreased gradually to the depth of 700 μm, which was consistent with the results obtained from OCT (Fig. 6f).

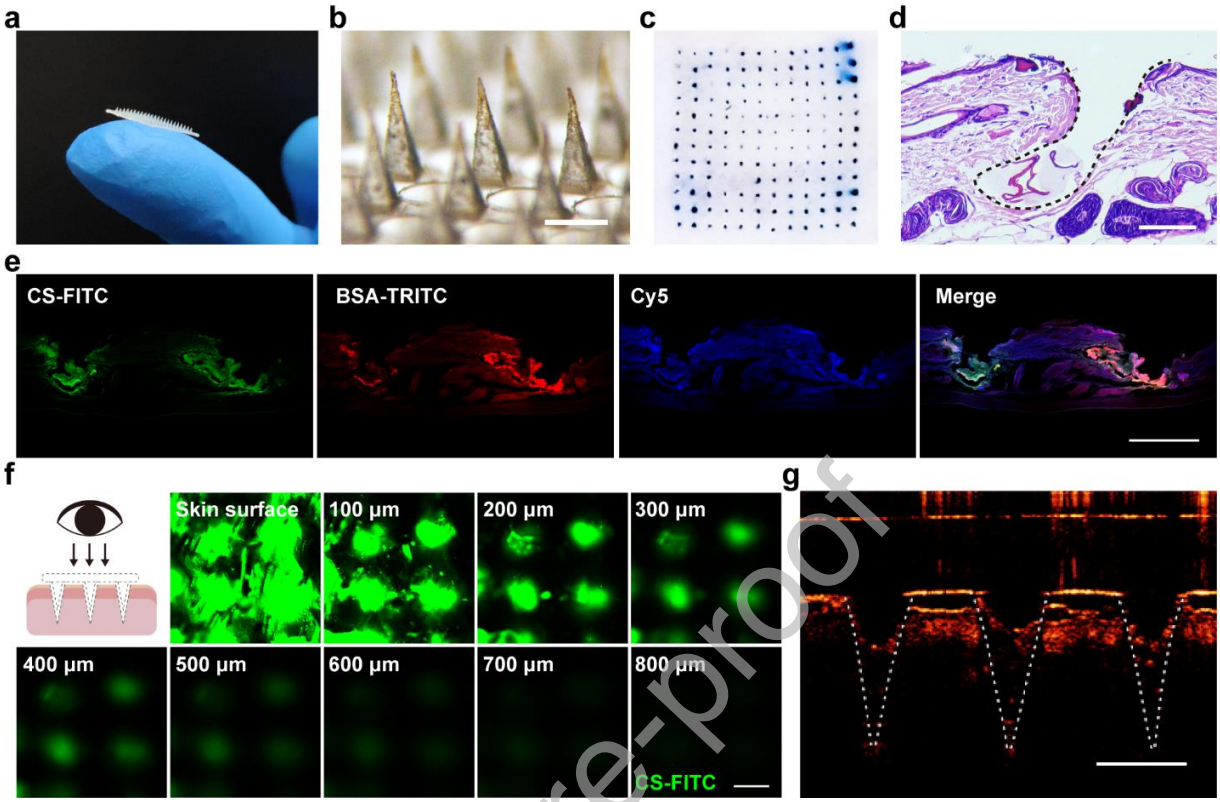

Fig. 6.

3.4. *In vitro* skin permeation study

The 1-MT amounts in CS-CSMN, ALG-CSMN and nMN were similar, demonstrating that the shell structure had little effect on 1-MT loading in microneedles (Fig. 7a). The influence of shell on transdermal delivery efficiency of microneedles was investigated using a Franz diffusion cell apparatus. As shown in Fig. 7b, the cumulative permeation rates across the rat abdomen skin of 1-MT released from three different microneedles were all more than 70% in 24 h, where CS-CSMN appeared to offer the highest rate. This could be explained that ALG-CSMN and nMN might soften or dissolve too quickly in the tissue fluid during the insertion process, while the slightly soluble chitosan shell could keep the needles intact and strong to go further down. The chitosan shell was still kept intact after CS-CSMN immersed in deionized water for five days (Fig. S5). The deeper depth could shorten the permeation distance of 1-MT in the skin and ultimately accelerate its permeation rate [35].

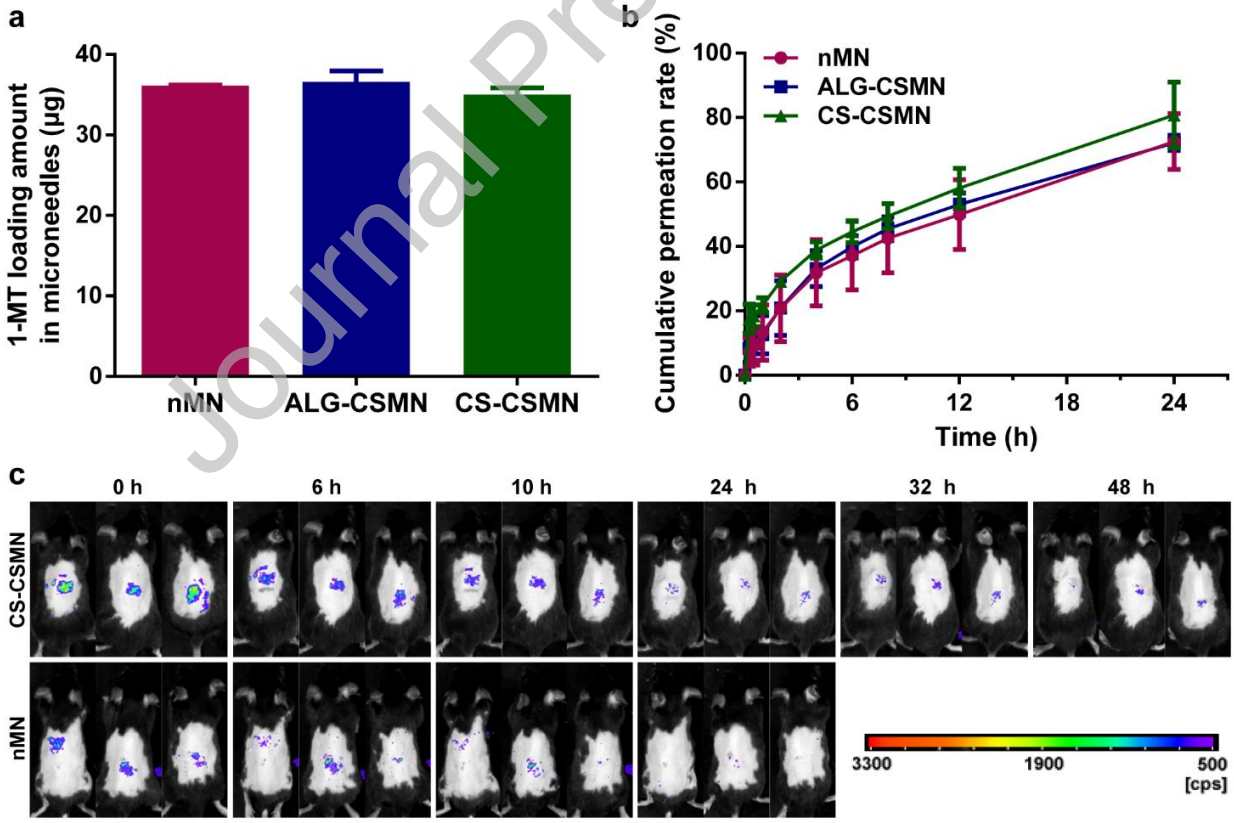

Fig. 7.

3.5. Protein retention time and chitosan shell degradation in skin

To investigate the influence of shell on the transdermal delivery efficiency of proteins, the real-time changes of BSA-TRITC fluorescence intensity in the skin after administration of nMN and CS-CSMN containing equivalent BSA-TRITC amount was monitored (Fig. 7c and S6). The initial fluorescence intensity of CS-CSMN group was significantly higher than that of nMN group after administration which could be explained by the better distribution of BSA-TRITC in CS-CSMN than that in nMN. BSA-TRITC was mainly concentrated at the needles tips of CSMN, while it was found near the needles bottom of nMN (Fig. 5a and 5b). The proteins distributed in the needles tips could be completely delivered into skin and wouldn't be affected by the elastic deformation of skin. The proteins distributed close to the base portion of nMN might remain on the surface of skin and be wiped away after administration of nMN, which resulted in lower transdermal delivery efficiency [34]. The fluorescence intensity of CS-CSMN inserted site gradually decreased over time and almost no fluorescence intensity could be detected after 48 hours, indicating the complete release of BSA-TRITC from CS-CSMN and permeation from skin to subcutaneous site.

Chitosan was water insoluble and biodegradable. To prove that chitosan shell could be degraded in skin, the degradation time of chitosan shell in skin was also investigated. As shown in Fig. S7, the fluorescence intensity of CS-FITC in skin was hardly detected after 48 hours, demonstrating the complete degradation of chitosan shell.

3.6. *In vivo* anti-tumor efficacy and safety

The anti-tumor efficacy of CS-CSMN was evaluated using subcutaneous melanoma mice model compared to intra-tumor injection route. Mice treated by aPD-L1/1-MT CS-CSMN exhibited slower tumor growth rate than those treated by intra-tumor injection of aPD-L1/1-MT solution (Fig. 8b and 8e). The better anti-tumor efficacy of CS-CSMN might be attributed to the continual permeation of drug from the skin to the tumor and prolonged residence time at the tumor sites, while the solution injected into the tumor couldn't be retarded in the tumor site and might drain to the subcutaneous space before it worked. Slower tumor growth rate was correlated with longer survival time. Administration of aPD-L1/1-MT CS-CSMN extended the survival times of tumor bearing mice (Fig. 8c). Although intra-tumor injection could reduce the tumor growth rate in the early time, the tumor grew fast in later period, which resulted in unimproved survival time. Neither obvious weight loss nor evidence of toxicity or inflammation in major organs was observed in all groups during experiment, indicating that CS-CSMN was a safe technique (Fig. 8d and 8i). CS-CSMN was also a low invasive administration form with skin roughly recovering in 3 h after administration (Fig. 8h).

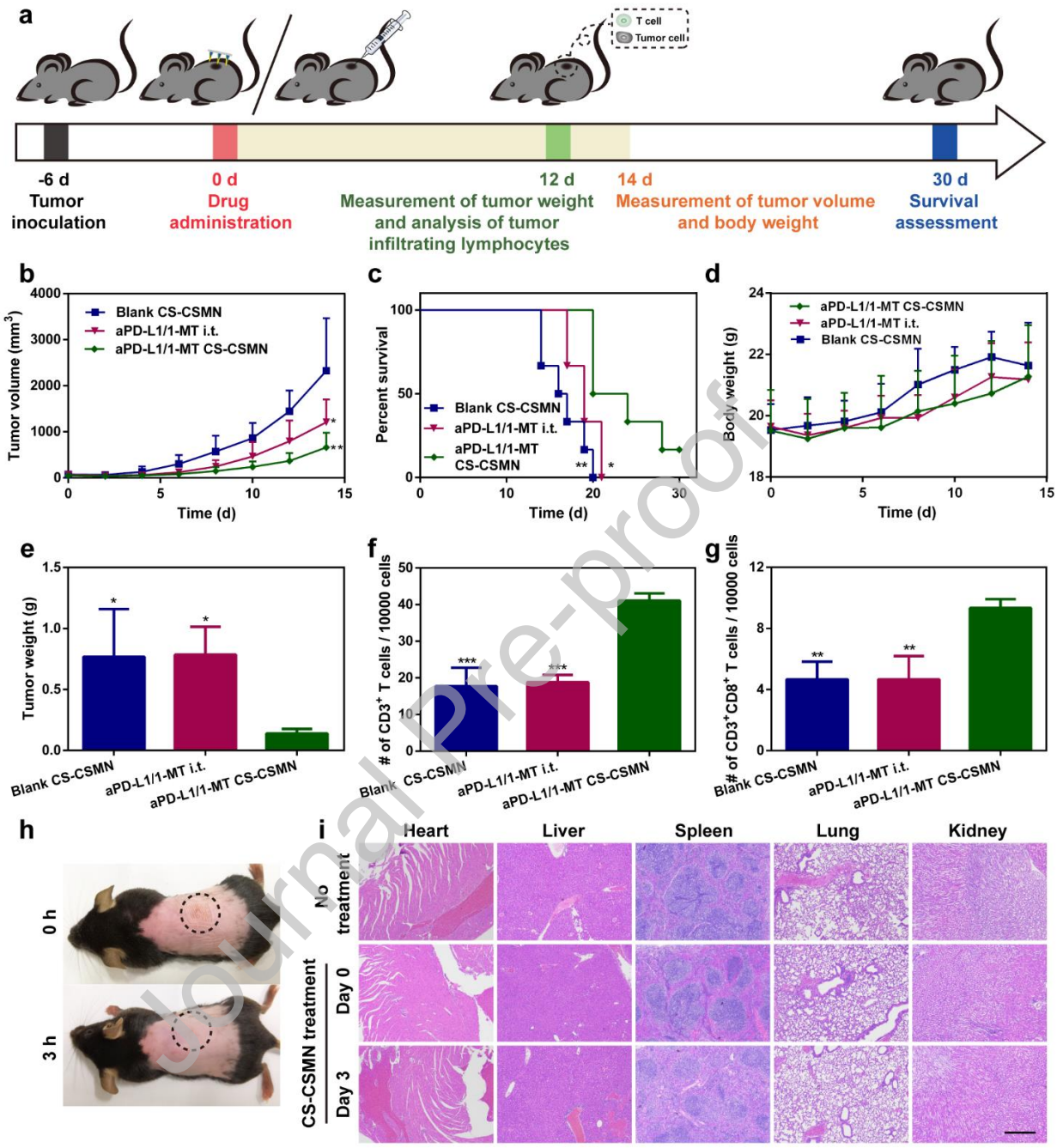

Fig. 8.

It is known that human immune system has the potential to kill cancer cells by activating T-cells. Upon activation, $CD4^+$ T cells produce cytokines that help $CD8^+$ T cells to fully mature.

Upon full maturation, $CD8^+$ T cells in turn proliferate, migrate to the tumor site and then lyse tumor cells, potentially mediating an anti-tumor response. To reveal the mechanisms mediating tumor regression, we further investigated the infiltration of immune cells into the tumor site 12 days after different treatments. The tumor site of aPD-L1/1-MT CS-CSMN group exhibited the highest infiltration of T lymphocytes including cytotoxic T lymphocytes ($CD3^+$ $CD8^+$), which was about 2-fold as compared with that of blank CS-CSMN control group (Fig. 8f and 8g). Intra-tumor injection of aPD-L1/1-MT solution failed to increase infiltration of T lymphocytes into the tumor site, showing similar population of $CD3^+$ and $CD3^+CD8^+$ T cells compared with blank CS-CSMN control group. In contrast to reports in other literatures, the modest effect of intra-tumor injection to increase immune cells infiltration might be attributed to the single administration with lower dose in this study [27]. The efficient delivery of aPD-L1 and 1-MT to tumor by CS-CSMN increased the infiltration of immune cells into the tumor site leading to the decrease in the tumor weight (Fig. 8e).

4. Conclusions

In summary, a highly drug-concentrated CSMN system was developed to achieve co-delivery of biomacromolecules and small molecules. The amounts of aPD-L1 and 1-MT loaded in microneedles were successfully increased by taking advantage of electrostatic interactions with charged shell and hydrogen-bond interaction with microneedle matrix materials. Using the preparation process described above, aPD-L1 was concentrated in the tips of microneedles, beneficial to its efficient transdermal delivery. The anti-tumor efficacy of aPD-L1 and 1-MT delivered by the microneedle system was better than that of intra-tumor injection route likely due to the longer local retention time in the tumor site. These results indicated that this CSMN

system could serve as a potential local co-delivery platform to deliver biomacromolecular drugs and other drugs simultaneously, not only for immunotherapy, but also for various diseases where combination therapy is required.

Acknowledgement

The authors appreciated the financial support from the National Natural Science Foundation of China (81803466, 81803467), the Foundation of Traditional Chinese Medicine Bureau of Guangdong Province (20191057), and the China Postdoctoral Science Foundation Founded Project (2018M633259).

Conflicts of interest

The authors declare no conflict of interest.

Declaration of Competing Interest

The authors declare that they have no known competing financial interests or personal relationships that could have appeared to influence the work reported in this paper.

References

[1] J. Ferlay, I. Soerjomataram, R. Dikshit, S. Eser, C. Mathers, M. Rebelo, D.M. Parkin, D. Forman, F. Bray, Cancer incidence and mortality worldwide: sources, methods and major patterns in GLOBOCAN 2012, Int. J. Cancer 136(5) (2015) E359-86.

[2] F. Bray, J. Ferlay, I. Soerjomataram, R.L. Siegel, L.A. Torre, A. Jemal, Global cancer statistics 2018: GLOBOCAN estimates of incidence and mortality worldwide for 36 cancers in 185 countries, Ca-Cancer J. Clin. 68(6) (2018) 394-424.

[3] K.M. Hargadon, Strategies to improve the efficacy of dendritic cell-based immunotherapy for melanoma, Front. Immunol 8 (2017) 1594.

[4] H. Kupcova Skalnikova, J. Cizkova, J. Cervenka, P. Vodicka, Advances in proteomic techniques for cytokine analysis: focus on melanoma research, Int. J. Mol. Sci. 18(12) (2017).

[5] M.E. Keir, M.J. Butte, G.J. Freeman, A.H. Sharpel, PD-1 and its ligands in tolerance and immunity, Annu. Rev. Immunol. 26 (2008) 677-704.

[6] D.F. McDermott, M.B. Atkins, PD-1 as a potential target in cancer therapy, Cancer Med.-Us 2(5) (2013) 662-673.

[7] D. Mittal, M.M. Gubin, R.D. Schreiber, M.J. Smyth, New insights into cancer immunoediting and its three component phases--elimination, equilibrium and escape, Curr. Opin. Immunol. 27 (2014) 16-25.

[8] N. Frydenlund, M. Mahalingam, PD-L1 and immune escape: insights from melanoma and other lineage-unrelated malignancies, Hum. Pathol. 66 (2017) 13-33.

[9] J.A. Seidel, A. Otsuka, K. Kabashima, Anti-PD-1 and anti-CTLA-4 therapies in cancer: mechanisms of action, efficacy, and limitations, Front. Oncol. 8 (2018) 86.

[10] H.O. Alsaab, S. Sau, R. Alzhrani, K. Tatiparti, K. Bhise, S.K. Kashaw, A.K. Iyer, PD-1 and PD-L1 checkpoint signaling inhibition for cancer immunotherapy: mechanism, combinations, and clinical outcome, Front. Pharmacol. 8 (2017).

[11] Y.W. Moon, J. Hajjar, P. Hwu, A. Naing, Targeting the indoleamine 2,3-dioxygenase pathway in cancer, J. Immunother. Cancer 3 (2015) 51.

[12] C. Robert, J. Schachter, G.V. Long, A. Arance, J.J. Grob, L. Mortier, A. Daud, M.S. Carlino, C. McNeil, M. Lotem, J. Larkin, P. Lorigan, B. Neyns, C.U. Blank, O. Hamid, C. Mateus, R. Shapira-Frommer, M. Kosh, H. Zhou, N. Ibrahim, S. Ebbinghaus, A. Ribas, Pembrolizumab versus ipilimumab in advanced melanoma, New Engl. J. Med. 372(26) (2015) 2521-2532.

[13] P.A. Ascierto, G.A. McArthur, Checkpoint inhibitors in melanoma and early phase development in solid tumors: what's the future?, J. Transl. Med. 15(1) (2017) 173.

[14] M. Mandala, C. Tondini, B. Merelli, D. Massi, Rationale for new checkpoint inhibitor combinations in melanoma therapy, Am. J. Clin. Dermatol. 18(5) (2017) 597-611.

[15] E. Fox, T. Oliver, M. Rowe, S. Thomas, Y. Zakharia, P.B. Gilman, A.J. Muller, G.C. Prendergast, Indoximod: an immunometabolic adjuvant that empowers T cell activity in cancer, Front. Oncol. 8 (2018).

[16] Y. Zakharia, O. Rixe, J.H. Ward, J.J. Drabick, M.F. Shaheen, M.M. Milhem, Phase 2 trial of the IDO pathway inhibitor indoximod plus checkpoint inhibition for the treatment of patients with advanced melanoma, J. Clin. Oncol. 36(15) (2018).

[17] S.L. Topalian, F.S. Hodi, J.R. Brahmer, S.N. Gettinger, D.C. Smith, D.F. McDermott, J.D. Powderly, R.D. Carvajal, J.A. Sosman, M.B. Atkins, P.D. Leming, D.R. Spigel, S.J. Antonia, L. Horn, C.G. Drake, D.M. Pardoll, L. Chen, W.H. Sharfman, R.A. Anders, J.M. Taube, T.L. McMiller, H. Xu, A.J. Korman, M. Jure-Kunkel, S. Agrawal, D. McDonald, G.D. Kollia, A. Gupta, J.M. Wigginton, M. Sznol, Safety, activity, and immune correlates of anti-PD-1 antibody in cancer, New Engl. J. Med. 366(26) (2012) 2443-54.

[18] H. Marwah, T. Garg, A.K. Goyal, G. Rath, Permeation enhancer strategies in transdermal drug delivery, Drug. deliv. 23(2) (2016) 564-78.

[19] W. Chen, R. Tian, C. Xu, B.C. Yung, G. Wang, Y. Liu, Q. Ni, F. Zhang, Z. Zhou, J. Wang, G. Niu, Y. Ma, L. Fu, X. Chen, Microneedle-array patches loaded with dual mineralized protein/peptide particles for type 2 diabetes therapy, Nat. Commun. 8(1) (2017) 1777.

[20] S. Yang, F. Wu, J. Liu, G. Fan, W. Welsh, H. Zhu, T. Jin, Phase-transition microneedle patches for efficient and accurate transdermal delivery of insulin, Adv. Funct. Mater. 25(29) (2015) 4633-4641.

[21] J. Yu, Y. Zhang, W. Sun, A.R. Kahkoska, J. Wang, J.B. Buse, Z. Gu, Insulin-responsive glucagon delivery for prevention of hypoglycemia, Small (2017).

[22] J. Arya, M.R. Prausnitz, Microneedle patches for vaccination in developing countries, J. Control. Release 240 (2016) 135-141.

[23] L. Dong, Y. Li, Z. Li, N. Xu, P. Liu, H. Du, Y. Zhang, Y. Huang, J. Zhu, G. Ren, J. Xie, K. Wang, Y. Zhou, C. Shen, J. Zhu, J. Tao, Au nanocage-strengthened dissolving microneedles for chemo-photothermal combined therapy of superficial skin tumors, ACS Appl. Mater. Interfaces 10(11) (2018) 9247-9256.

[24] P. Pei, F. Yang, J. Liu, H. Hu, X. Du, N. Hanagata, S. Zhao, Y. Zhu, Composite-dissolving microneedle patches for chemotherapy and photothermal therapy in superficial tumor treatment, Biomater. Sci. (2018).

[25] M.C. Chen, Z.W. Lin, M.H. Ling, Near-infrared light-activatable microneedle dystem for treating superficial tumors by combination of chemotherapy and photothermal therapy, ACS Nano 10(1) (2016) 93-101.

[26] C. Wang, Y. Ye, G.M. Hochu, H. Sadeghifar, Z. Gu, Enhanced cancer immunotherapy by microneedle patch-assisted delivery of anti-PD1 antibody, Nano Lett. 16(4) (2016) 2334-40.

[27] Y. Ye, J. Wang, Q. Hu, G.M. Hochu, H. Xin, C. Wang, Z. Gu, Synergistic transcutaneous immunotherapy enhances antitumor immune responses through delivery of checkpoint inhibitors, ACS Nano 10(9) (2016) 8956-63.

[28] Q.Q. Wang, G.T. Yao, P. Dong, Z.H. Gong, G. Li, K.J. Zhang, C.B. Wu, Investigation on fabrication process of dissolving microneedle arrays to improve effective needle drug distribution, Eur. J. Pharm. Sci. 66 (2015) 148-156.

[29] G.T. Yao, G.L. Quan, S.Q. Lin, T.T. Peng, Q.Q. Wang, H. Ran, H.P. Chen, Q. Zhang, L.L. Wang, X. Pan, C.B. Wu, Novel dissolving microneedles for enhanced transdermal delivery of levonorgestrel: In vitro and in vivo characterization, Int. J. Pharmaceut. 534(1-2) (2017) 378-386.

[30] S. Xu, W.G. Dai, Drug precipitation inhibitors in supersaturable formulations, Int. J. Pharmaceut. 453(1) (2013) 36-43.

[31] M. Dangol, S. Kim, C.G. Li, S. Fakhraei Lahiji, M. Jang, Y. Ma, I. Huh, H. Jung, Anti-obesity effect of a novel caffeine-loaded dissolving microneedle patch in high-fat diet-induced obese C57BL/6J mice, J. Control. Release (2017).

[32] R.F. Donnelly, R. Majithiya, T.R. Singh, D.I. Morrow, M.J. Garland, Y.K. Demir, K. Migalska, E. Ryan, D. Gillen, C.J. Scott, A.D. Woolfson, Design, optimization and characterisation of polymeric microneedle arrays prepared by a novel laser-based micromoulding technique, Pharm Res 28(1) (2011) 41-57.

[33] Y. Zhang, J. Wang, J. Yu, D. Wen, A.R. Kahkoska, Y. Lu, X. Zhang, J.B. Buse, Z. Gu, Bioresponsive Microneedles with a sheath structure for H_2O_2 and pH cascade-triggered insulin delivery, Small (2018).

[34] M.C. Chen, M.H. Ling, S.J. Kusuma, Poly-gamma-glutamic acid microneedles with a supporting structure design as a potential tool for transdermal delivery of insulin, Acta. Biomater. 24 (2015) 106-116.

[35] C. Uppuluri, A.S. Shaik, T. Han, A. Nayak, K.J. Nair, B.R. Whiteside, B.N. Nalluri, D.B. Das, Effect of microneedle type on transdermal permeation of rizatriptan, Aaps Pharmscitech 18(5) (2017) 1495-1506.

Figure captions:

Fig. 1. Schematic illustration of CSMN-assisted co-delivery of aPD-L1 and 1-MT for melanoma immunotherapy.

Fig. 2. Schematic illustration of CSMN preparation process.

Fig. 3. Effect of polymers on the inhibition of 1-MT crystallization in its supersaturated solutions. (a) Apparent concentration-time profiles obtained from 1-MT supersaturated solutions containing different polymers (Mean±SD, *n*=3). (b) Apparent concentration-time profiles obtained from 1-MT supersaturated solutions with different original concentrations of 1-MT and PVA (Mean±SD, *n*=3). (c) Polarized light microscopy images of 1-MT solution with different polymers at crystallization state after preparation (scale bar: 200 μm).

Fig. 4. CS-CSMNs with shells prepared using different concentrations of chitosan solution and their BSA loading efficiencies. (a) Fluorescence images of CS-CSMN with shells prepared using different concentrations of CS-FITC solution captured by stereo fluorescence microscope (scale bar: 500 μm). (b) Fluorescence images of cross-sections of CS-CSMN with shells prepared using different concentrations of CS-FITC solution obtained by confocal laser scanning along z axis from tip to base of CS-CSMN (scale bar: 150 μm). (c) Loading efficiencies of BSA in CS-CSMNs with shells prepared using different concentrations of chitosan solution (Mean±SD, *n*=3).

Fig. 5. Loading efficiency of protein in nMN, CS-CSMN and ALG-CSMN. (a) Fluorescence images of cross-sections of three BSA-FITC loaded microneedles obtained by confocal laser scanning along z axis from tip to base of microneedles (scale bar: 300 μm). (b) Fluorescence images of three BSA-FITC loaded microneedles obtained by stereo fluorescence microscope (scale bar: 500 μm). (c) Loading efficiency of aPD-L1 in three different microneedles (Mean±SD, *n*=3). (d) Fluorescence microscopy images of drug loaded CS-CSMN (scale bar: 500 μm).

Fig. 6. Skin insertion ability of CS-CSMN. (a) Photograph of a representative CS-CSMN patch. (b) Bright-field micrograph of CS-CSMN (scale bar: 500 μm). (c) A representative image of excised rat abdominal skin after CS-CSMN insertion followed by trypan blue staining. (d) H&E-stained cross-section of rat skin following application of CS-CSMN (scale bar: 100 μm). (e) Fluorescence images of cross-sectional excised rat abdominal skin penetrated by fluorescent CS-CSMN (scale bar: 300 μm). (f) Fluorescence images of cross-sections of excised rat abdominal skin penetrated by CSMN with CS-FITC shell, obtained by confocal laser scanning along z axis from surface to depth of skin (scale bar: 300 μm). (g) A representative OCT image of excised rat abdominal skin at 1 min after CS-CSMN insertion (scale bar: 500 μm).

Fig. 7. Transdermal delivery efficiencies of CSMNs. (a) Loading amounts of 1-MT in three different microneedles (Mean±SD, *n*=3). (b) Cumulative permeation rate across rat abdomen skin of 1-MT released from three different microneedles (Mean±SD, *n*=3). (c) *In vivo* fluorescence imaging of mice treated by BSA-TRITC loaded CS-CSMN and nMN at different time points.

Fig. 8. *In vivo* antitumor efficacy and safety of aPD-L1 and 1-MT delivered by CS-CSMN in B16 Melanoma C57BL/6 mice. (a) Schematic illustration of CS-CSMN anti-tumor study. Tumor volume (b), survival rate (c) and body weight (d) of mice after different treatments (Mean±SD, *n*=6). (e) Tumor weight and absolute numbers of (f) $CD3^+$ T cells and (g) $CD3^+CD8^+$ T cells per 10000 of cells in tumor tissue after the removal of red blood cells 12 days after treatment (Mean±SD, *n*=3). (h) Photographs of mouse back skin after CS-CSMN insertion. (i) H&E-stained cross-sections of mice major organs (scale bar: 400 μm).

Graphical abstract